Electronic Supplementary Information

Tailoring charge reconfiguration in dodecahedral Co_2P@carbon nanohybrid by triple-doping engineering for promoted reversible oxygen catalysis

Luhan Li[a], Lei Zhang[a,*], Zhicheng Nie[a], Wenyu Ma[a], Nianpeng Li[a,b], Thomas Wågberg[c,*] and Guangzhi Hu[b,c,*]

[a] School of Materials Science and Engineering, State Key Laboratory of Mining Response and Disaster Prevention and Control in Deep Coal Mines, Anhui University of Science and Technology, Huainan, Anhui 232001, P.R. China.

[b] Institute for Ecological Research and Pollution Control of Plateau Lakes, School of Ecology and Environmental Science, Yunnan University, Kunming, Yunnan 650504, P.R. China.

[c] Department of Physics, Umeå University, Umeå S-901 87, Sweden.

Corresponding author. Tel.: +86-554-6668643; Fax: +86-554-6668643

E-mail: leizhang@aust.edu.cn (L. Zhang); guangzhihu@ynu.edu.cn (G. Hu); thomas.wagberg@umu.se (T. Wågberg)

Experimental section

Materials: zinc acetate dihydrate, cobalt acetate tetrahydrate, ferric nitrate hexahydrate, phytic acid, 2-methylimidazole, and methanol were purchased from Sigma-Aldrich. All reagents were of analytical grade and used as received.

Materials characterizations: The composition and crystalline phase of the sample were investigated with powder X-ray diffraction measurements (XRD, Shimadzu XRD-6000, Japan), X-ray photoelectron spectroscopy and ultraviolet photoemission spectroscopy (XPS and UPS, Thermo ESCALAB 250XI, America), as well as energy dispersive spectrometry (EDS, Hitachi S-4800 and JEM-2100, Japan). The morphology and microstructure of the product were observed with a scanning electron microscope (SEM, Hitachi S-4800, Japan) and a high resolution transmission electron microscope (TEM, JEM-2100, Japan). Raman spectra were recorded in the spectral range of 200-3200 cm^{-1} using a Raman spectromicroscope (LabRAM HR800, Horiba Jobin Yvon, France). The specific surface areas of the samples were determined from the N_2 sorption/desorption isotherms, based on the Brunauer-Emmett-Teller model, measured with a Micrometrics ASAP 2010.

Electrochemical characterizations:

The measurement of ORR and Zn-air battery: Each catalyst (10 mg) was dispersed into a solution (1.92 mL) containing ethanol/H_2O (1/1, v/v) and Nafion (5 wt%, 80 μL) by ultrasonication for 30 min for the following procedures. The ORR performances were evaluated on a CHI760D electrochemical analyzer using a standard three-electrode system. The glass carbon electrode after loading the catalyst was used as the working electrode. A carbon rod was used as the counter electrode for ORR tests. A saturated calomel electrode (SCE) was selected as the reference electrode. For ORR measurements, the dispersion (10 μL) was uniformly dropped onto a freshly polished glassy carbon electrode (4 mm in diameter), which was dried under ambient conditions. The electrochemical experiments were carried out in an O_2-saturated 0.1 M KOH electrolyte for the ORR. The potential cycling was repeated until the reproducible CV curves were obtained before the measurements. All current densities were normalized to the geometrical surface area and the measured potential *vs*. SCE was converted to the potential *vs*. the reversible hydrogen electrode (RHE). Rotating disk electrode (RDE) measurements were conducted at different rotating speeds from 400 to 1600 rpm, and rotating ring disk electrode (RRDE) (*ca*. 0.1256 cm^2 for the disk and *ca*. 0.0707 cm^2 for the ring) measurements were carried out at 1600 rpm. The electron transfer number (*n*) during ORR was estimated by measuring the diffusion-limiting current density (j_L) at different rotating speed (ω) of the working electrode according to equation 1 (Koutecky-Levich equation):

$$1/j = 1/j_L + 1/j_k = 1/(B\omega^{1/2}) + 1/j_k = 1/[(0.2nFC_0D_0^{2/3}\upsilon^{-1/6})\omega^{1/2}] + 1/j_k \qquad (1)$$

in which n is the number of electrons transferred in the reduction of one O_2 molecule; j, j_L and j_k are the measured current density, diffusion-limiting current densities and kinetic-limiting current density; F is the Faraday constant (F = 96485 C/mol); C_0 is the bulk concentration of O_2 in the solution ($C_0 = 1.2 \times 10^{-6}$ mol/cm^3); D_0 is the diffusion coefficient of O_2 in 0.1 M KOH ($D_0 = 1.9 \times 10^{-5}$ cm^2/s^1); υ is the kinematics viscosity of the electrolyte (υ = 0.01 cm^2/s^1).

The electron transfer number (*n*) could also be determined from RRDE measurements based on the disk current (I_d) and ring current (I_r) *via* the following equation 2:

$$n = 4 \times I_d/(I_d + I_r/N) \qquad (2)$$

The peroxide percentage (% HO_2^-) was calculated based on equation 3:

$$\% \, HO_2^- = 200 \times (I_r/N)/(I_d + I_r/N) \qquad (3)$$

Where N is the current collection efficiency of the Pt ring, 0.37.

Ni foams were carefully washed with HCl (1 M) and then rinsed with absolute ethanol and distilled water to remove any oxides on the surface. The catalyst (10 mg) was dispersed into a solution (1.92 mL) containing ethanol/H_2O (1/1, v/v) and Nafion (5 wt%, 80 μL) by ultrasonication for the following procedures. The resultant inks were carefully dropped onto the respective Ni foams and then kept in a vacuum container for 30 min. For the primary Zn-air battery, the loading amounts of the catalyst and Pt/C were 1 mg/cm^2, respectively. For the rechargeable Zn-air battery, the loading amount of the catalyst was 1 mg/cm^2, while the Pt/C and RuO_2 inks were mixed with a ratio of 1:3, and a total catalyst loading amount of 1 mg/cm^2 was obtained. The Zn-air battery was assembled with Zn powder, a 6 M KOH solution [mixed with 0.2 M $Zn(Ac)_2$ for rechargeable Zn-air battery], and an air cathode comprising a catalyst layer and gas-diffusion layer was used as a backing layer next to the Ni foam-based catalyst layer to prevent electrolyte leakage.

The measurement of OER: The OER activity of the product was characterized on a CHI760D electrochemical workstation with a typical 3-electrode setup. The working electrode was prepared using the as-prepared powders (85 wt%) as the active material and polyvinylidene fluoride (15 wt%) as the binder. They were mixed in N-methylpyrrolidone (NMP) to form a sample suspension. The working electrode was fabricated by drop-casting the sample suspension, sonicated for 30 min before use, onto a graphite electrode (1 cm × 1 cm), and dried at 80 °C in an oven. The mass loading of the active material on the working electrode was controlled to be around 0.5 mg/cm^2. A platinum foil counter electrode and a Hg/HgO reference electrode were employed to complete the

3-electrode setup. For the measurements, 1 M KOH (pH = 13.85) aqueous solution was used as the electrolyte. The potential values for the OER in this study were converted and referred to the reversible hydrogen electrode (RHE) using the Nernst equation: $E_{RHE} = E_{Hg/HgO} + 0.098 + 0.059pH$, where $E_{Hg/HgO}$ was the experimentally measured potential against the Hg/HgO reference electrode. All linear scan voltammetry (LSV) polarization curves were *iR*-corrected with respect to the involved solution resistances. The over-potential (η) was calculated using the equation: $\eta = E_{RHE} - 1.23$. Prior to electrochemical measurements, the working electrode was conditioned by cycling through the potential window of 0 to 0.8 V *vs.* Hg/HgO thirty times at a scan rate of 100 mV/s. The polarization curves were recorded with a linear potential sweep at a scan rate of 2 mV/s. The electrochemical impedance spectroscopy (EIS) was conducted in the frequency range of 10^5 to 0.01 Hz with an AC amplitude of 5 mV and the applied potential set at $E_{Hg/HgO} = 0.6$ V. The electrochemical active surface area (ECSA) of the catalysts was characterized from the double-layer charging curves obtained from cyclic voltammetry at increasing scan rates within a non-Faradaic potential window (0.895-0.995 V *vs.* RHE), in which no Faradaic redox reactions occur. Long-term stability test was carried out with chronopotentiometric measurements. For calculation of the turnover frequency (TOF), reductive negative scan peak areas were firstly determined from cyclic voltammograms recorded at a specific scan rate, for example, 300 mV/s. Charge (Q) can be obtained with the formula: Q = peak area/300 mV/s. Assuming a single-electron transfer reaction in the reduction process, the number of surface active sites (n) can be calculated with the equation: $n = Q/(1\times1.602\times10^{-19})$. Finally, TOF values were obtained from $TOF = j\times N_A/(4\times n\times F)$ (j = current density, N_A = Avogadro number, F = Faraday constant). The work function (W_F) could be obtained with the formula: $W_F = h\nu - (E_{cutoff} - E_F)$, where, $h\nu$ represented the energy of the incident photon (21.22 eV), E_{cutoff} was the onset level connected with the secondary edge, E_F was the Fermi level (E_F, set to 0 eV). W_F reflected the dynamics of electrons on the surface of the samples.

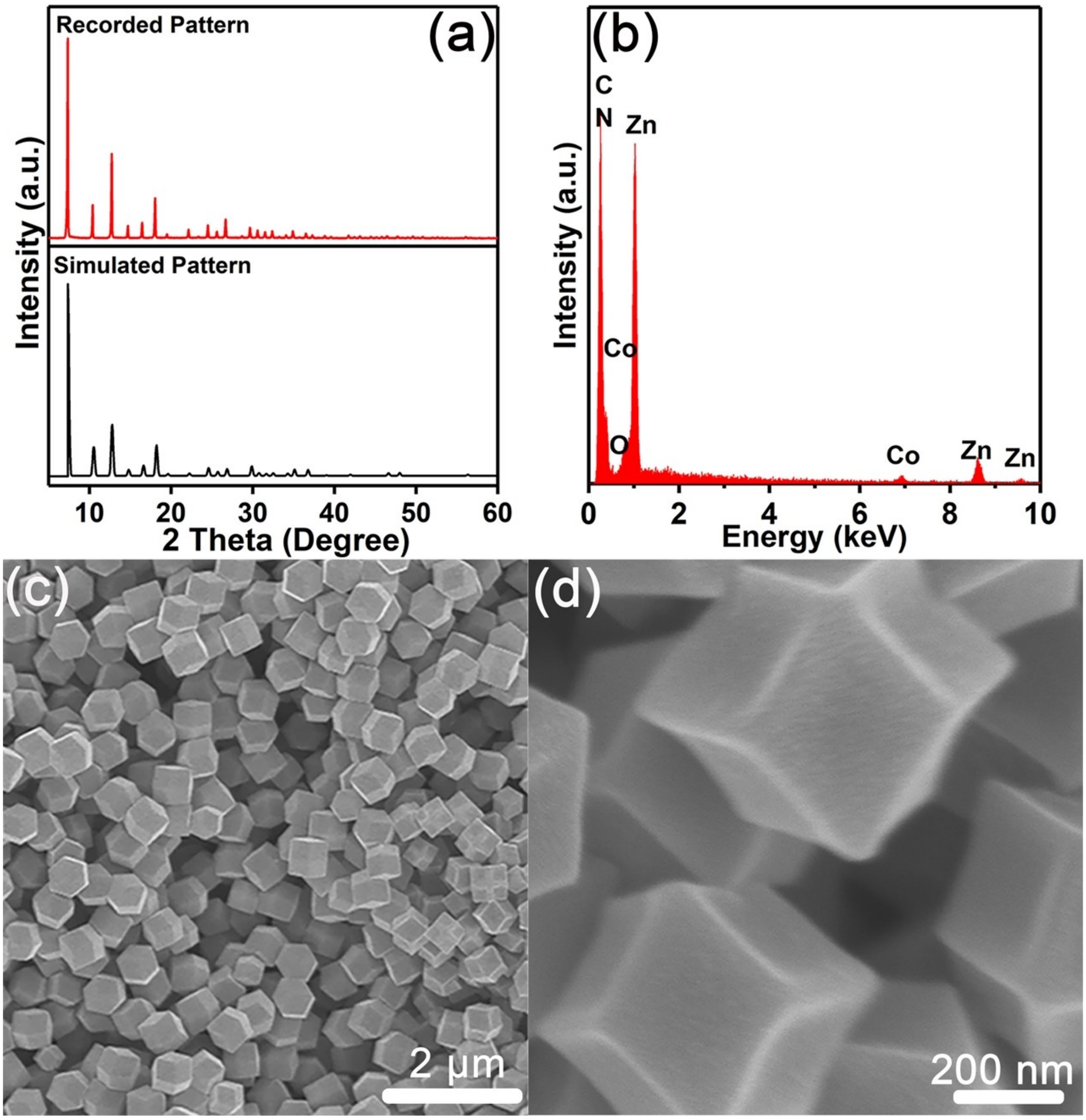

Figure S1 (a) XRD pattern, (b) EDS spectrum and (c-d) SEM images of the as-developed Zn/Co-ZIF dodecahedron.

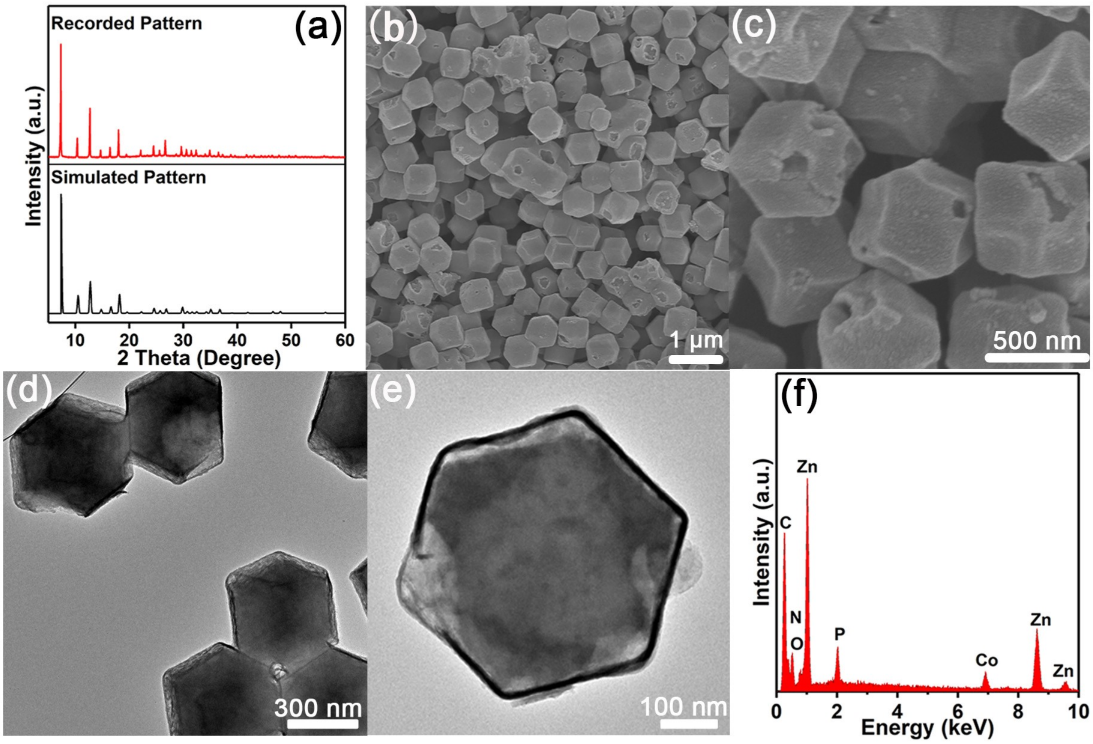

Figure S2 (a) XRD pattern, (b-c) SEM and (d-e) TEM images, as well as (f) the EDS spectrum of E-Zn/Co-ZIF dodecahedron.

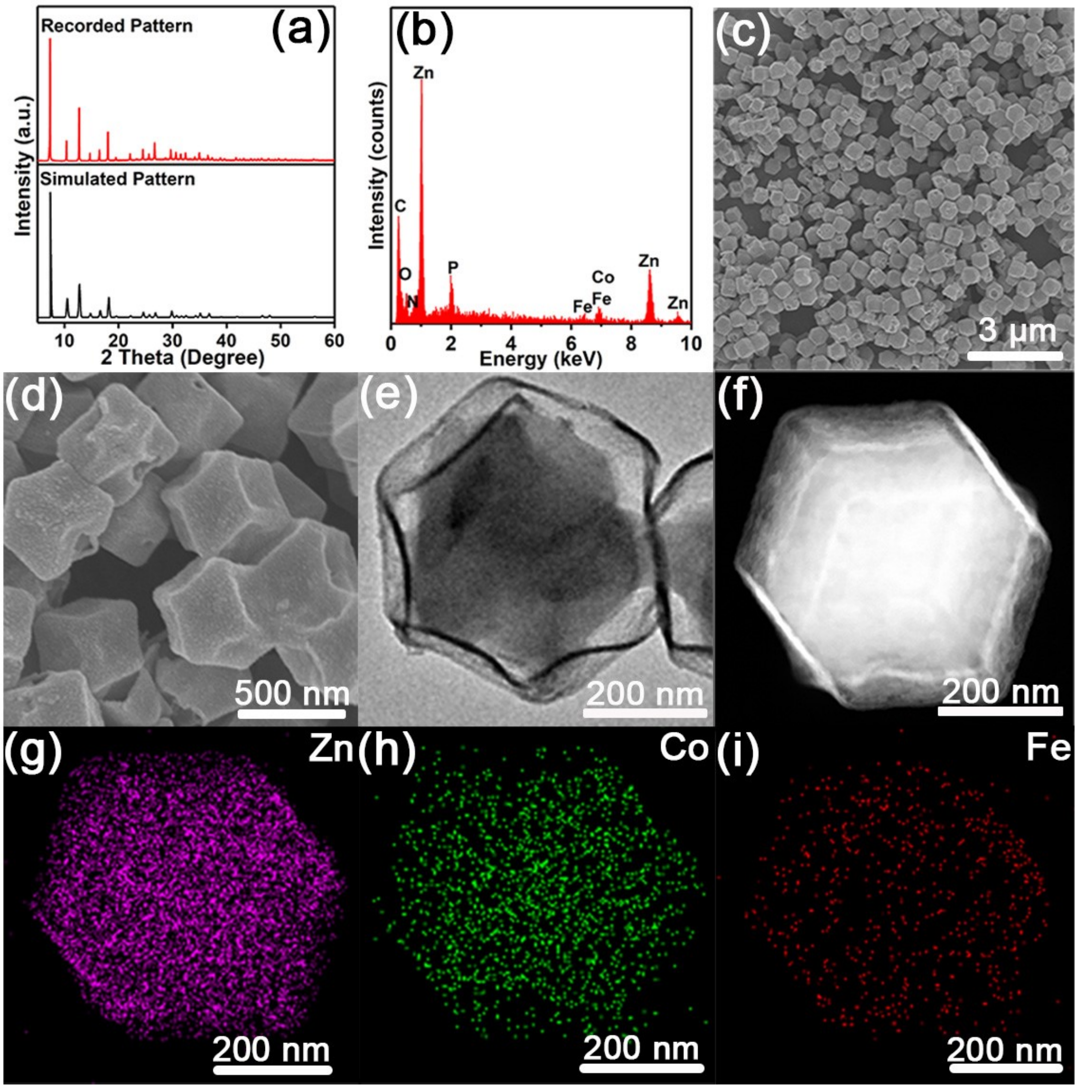

Figure S3 (a) XRD pattern, (b) EDS spectrum, (c-d) SEM and (e) TEM images, as well as (f-i) EDS elemental mapping of E-Zn/Co-ZIF-Fe dodecahedron.

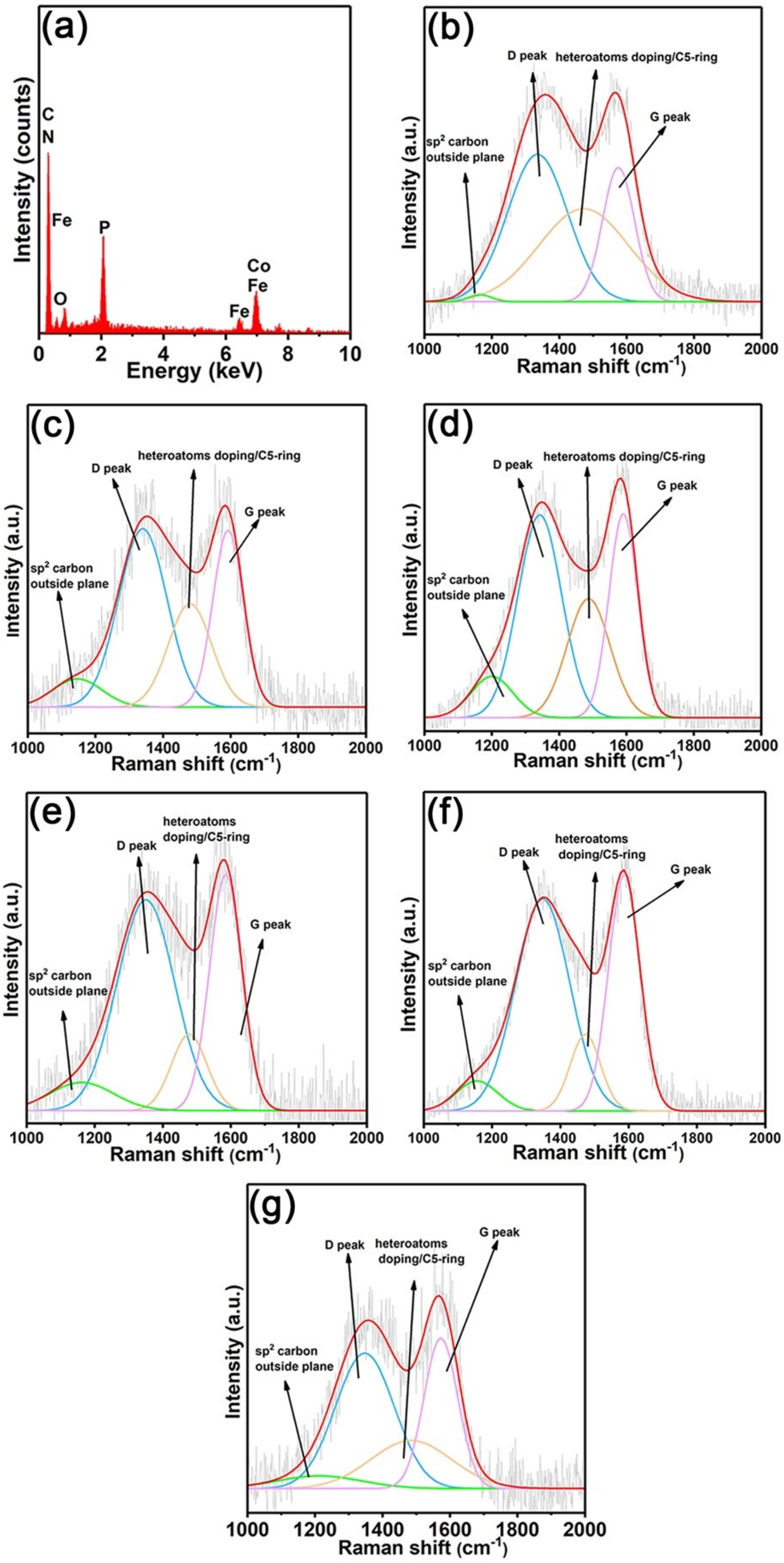

Figure S4 (a) EDS spectrum of the well-managed Fe-Co_2P@NPDC product; Raman spectra of (b) Fe-Co_2P@NPDC, (c) Fe-Co_2P@NPDC-2, (d) Fe-Co_2P@NPDC-1, (e) Co_2P-NPDC, (f) NPDC, and (g) NDC products.

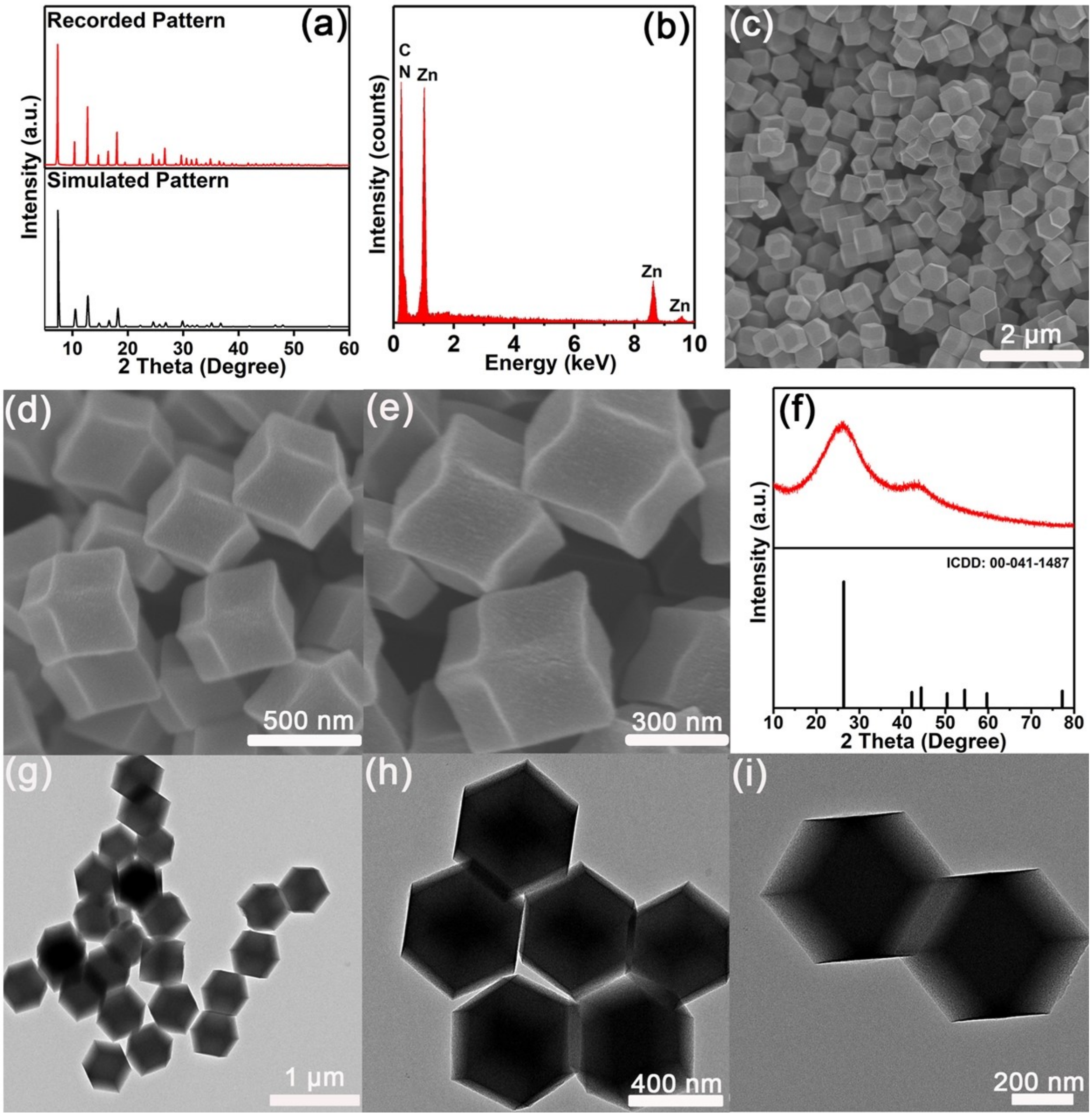

Figure S5 (a) XRD pattern, (b) EDS spectrum and (c-e) SEM images of Zn-ZIF dodecahedron; (f) XRD pattern, and (g-i) TEM images of NDC.

In order to prepare NDC, Zn-ZIF dodecahedron was constructed as a precursor (Figure S5a-S5e). After high temperature carbonization, an NDC sample was obtained, which could be confirmed by its XRD pattern, and TEM images, shown in Figure S5f-S5i.

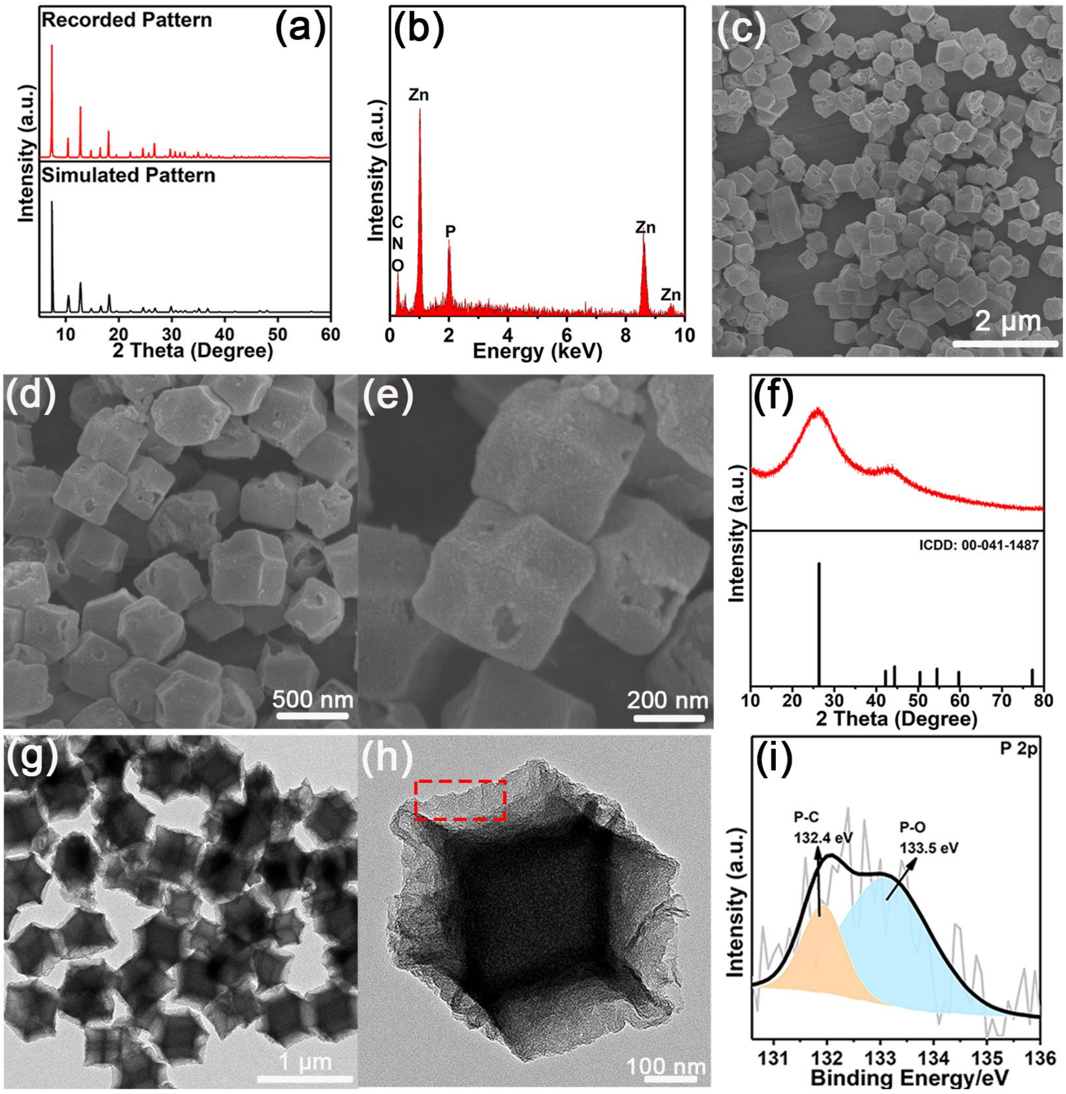

Figure S6 (a) XRD pattern, (b) EDS spectrum and (c-e) SEM images of E-Zn-ZIF dodecahedron; (f) XRD pattern, (g-h) TEM images and (i) XPS spectra of NPDC catalyst.

In order to prepare NPDC, Zn-ZIF dodecahedrons were then etched and doped with phytic acid (Figure S6a-S6e). After high temperature carbonization, an NPDC sample was obtained, which could be confirmed by its XRD pattern, TEM images and XPS spectrum, shown in Figure S6f-S6i.

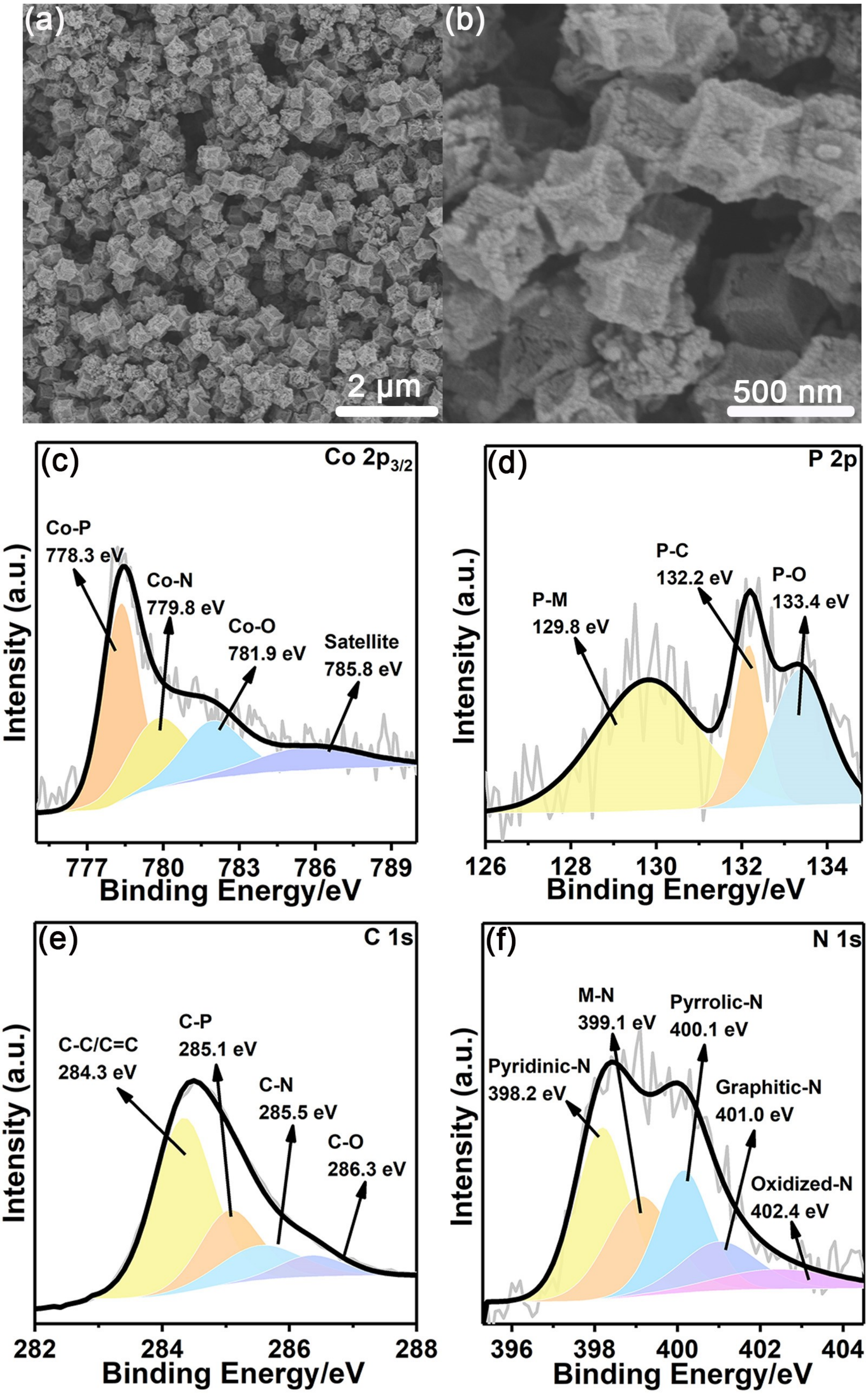

Figure S7 (a-b) SEM images and (c-f) XPS spectra of Co_2P@NPDC catalyst.

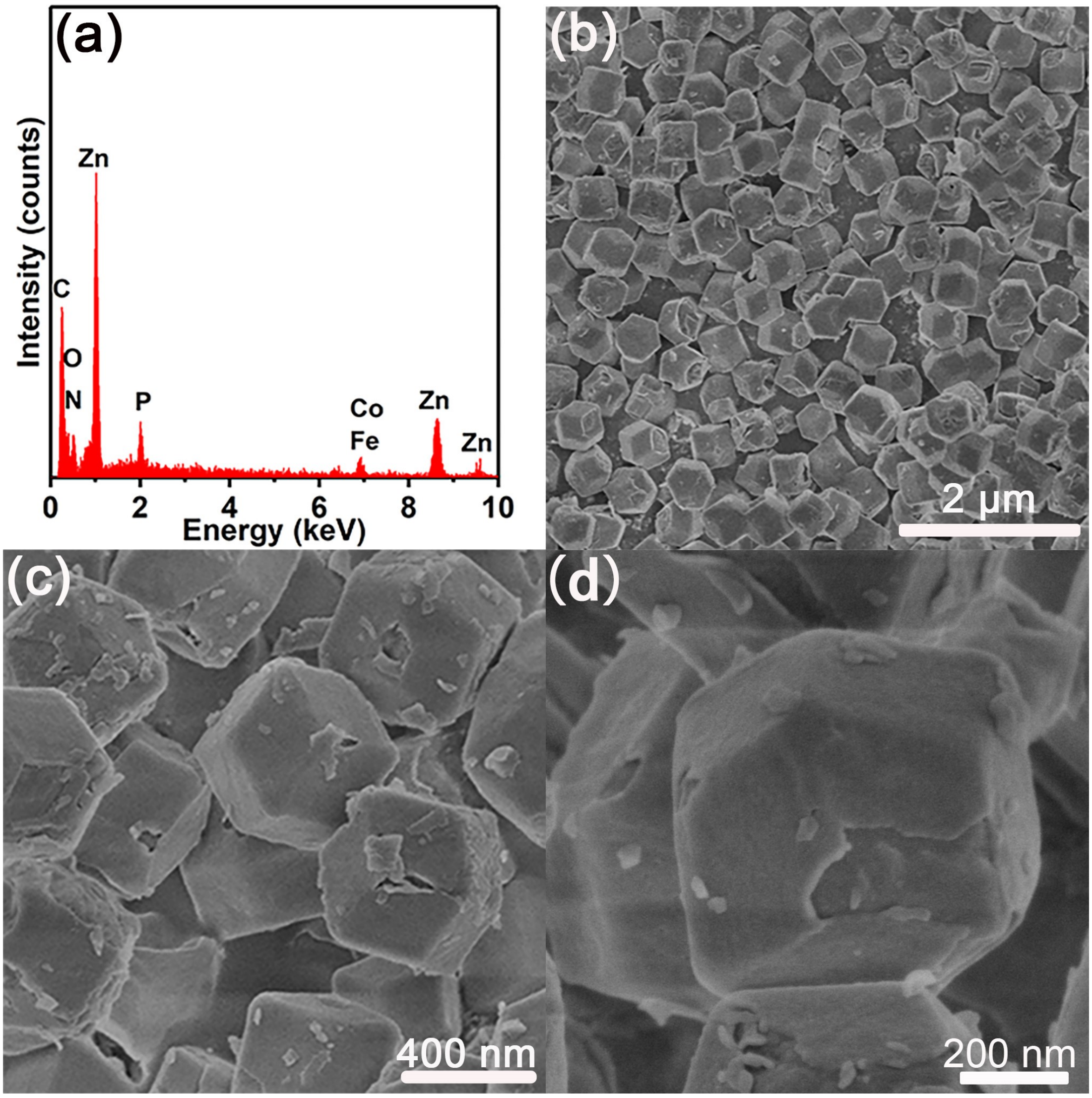

Figure S8 (a) EDS spectrum and (b-d) SEM images of E-Zn/Co-ZIF-Fe-1 dodecahedron.

As a comparison, 5 mg of $Fe(NO_3)_3·9H_2O$ was added into 20 mL of methanol solution containing 0.087 g of E-Zn/Co-ZIF, thus yielding the E-Zn/Co-ZIF-Fe-1 dodecahedron, as demonstrated in Figure S8.

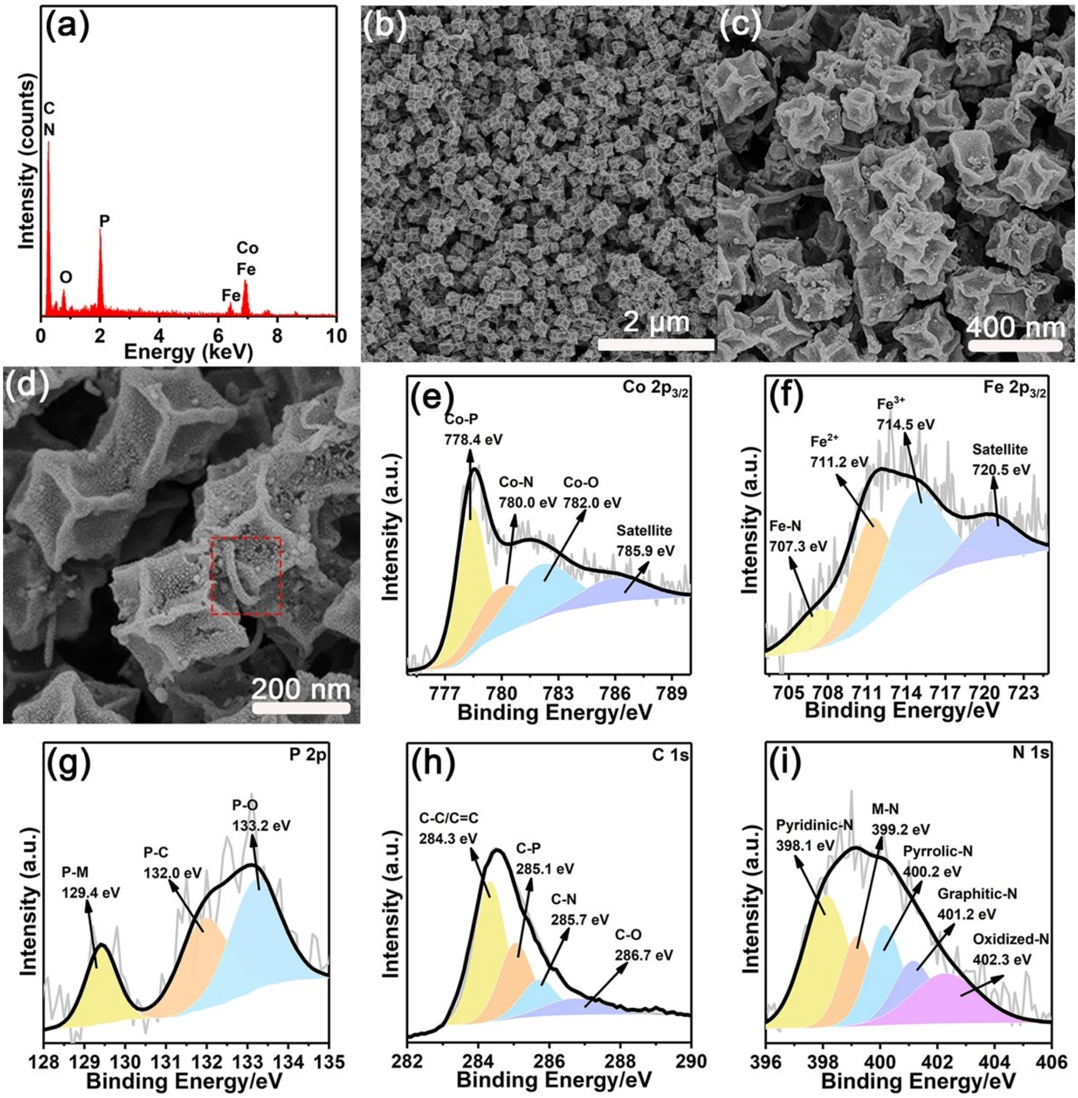

Figure S9 (a) EDS spectrum, (b-d) SEM images of Fe-Co_2P@NPDC-1 and (e-i) XPS spectra of Fe-Co_2P@NPDC-1 catalyst.

The following calcination procedure converted E-Zn/Co-ZIF-Fe-1 dodecahedrons into the desirable Fe-Co_2P@NPDC-1 product, as demonstrated in Figure S9. The calculated molar ratio of Co/Fe in the as-developed Fe-Co_2P@NPDC-1 is determined to be approximately 5.2:1.

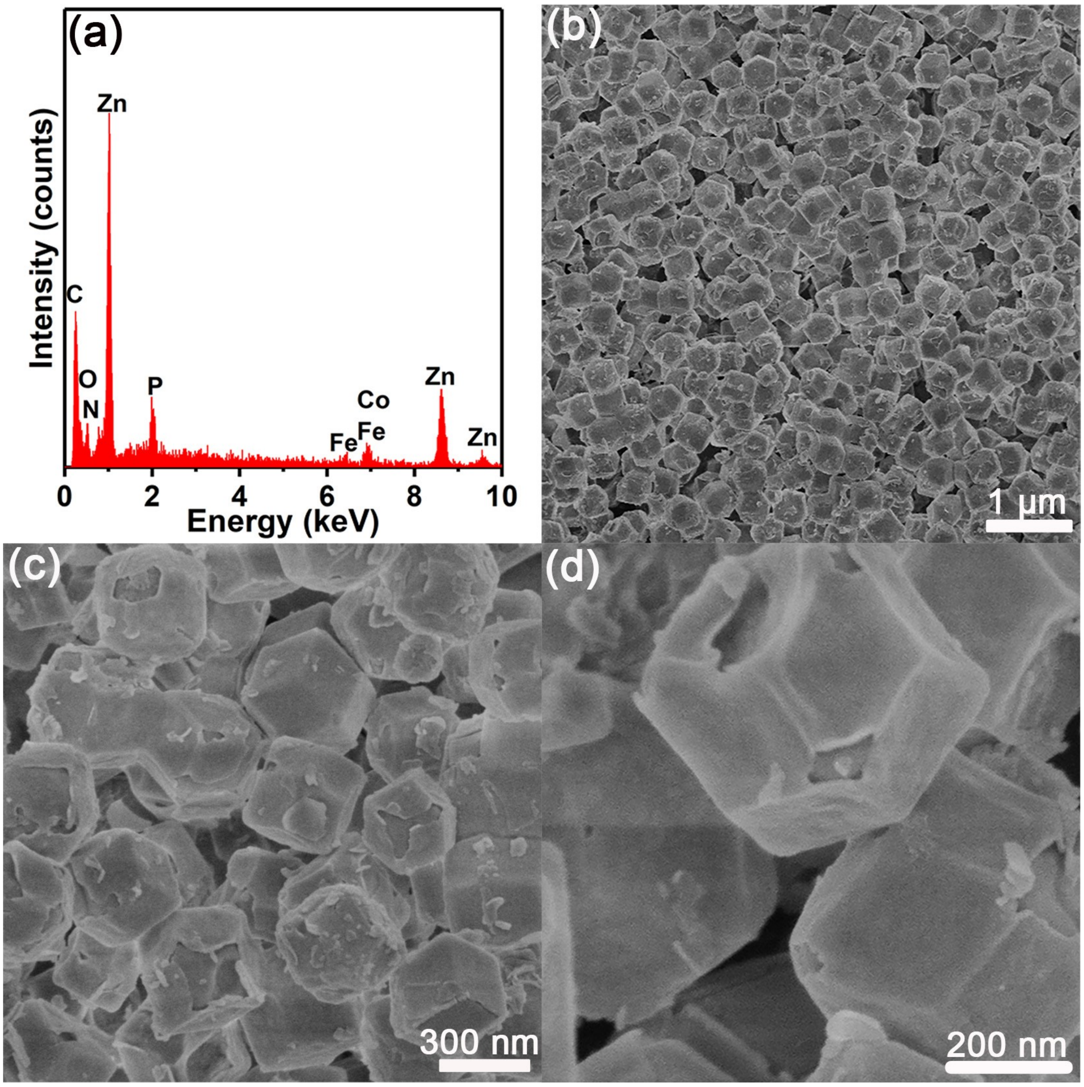

Figure S10 (a) EDS spectrum and (b-d) SEM images of E-Zn/Co-ZIF-Fe-2 dodecahedron.

As a comparison, 15 mg of $Fe(NO_3)_3 \cdot 9H_2O$ was added into 20 mL of methanol solution containing 0.087 g of E-Zn/Co-ZIF, thus yielding the E-Zn/Co-ZIF-Fe-2 dodecahedron, as demonstrated in Figure S10.

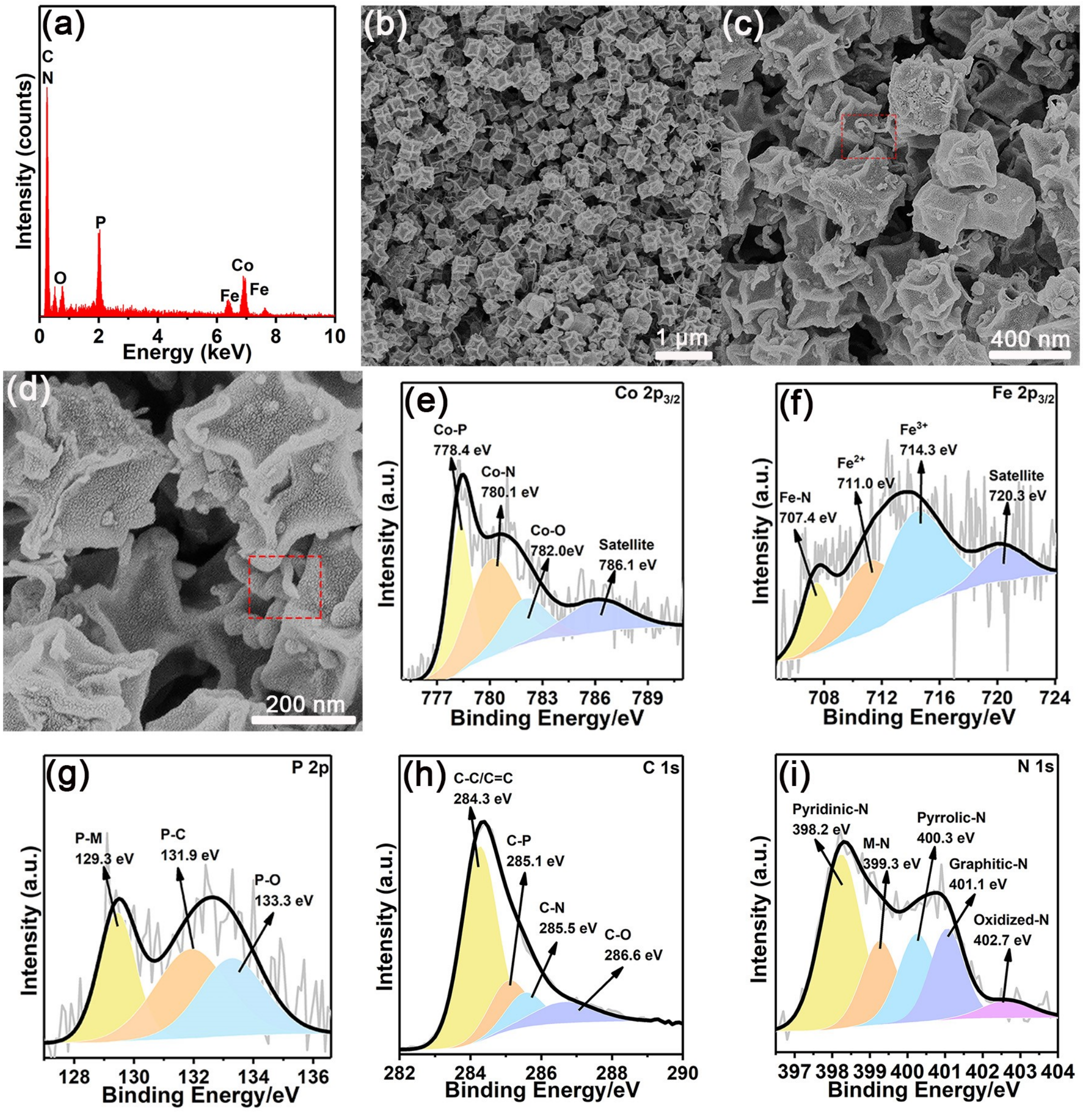

Figure S11 (a) EDS spectrum, (b-d) SEM images of Fe-Co_2P@NPDC-2 and (e-i) XPS spectra of Fe-Co_2P@NPDC-2 catalyst.

The following calcination procedure converted E-Zn/Co-ZIF-Fe-2 dodecahedrons into the desirable Fe-Co_2P@NPDC-2 product, as demonstrated in Figure S11. The calculated molar ratio of Co/Fe in the as-developed Fe-Co_2P@NPDC-2 is determined to be approximately 3.7:1.

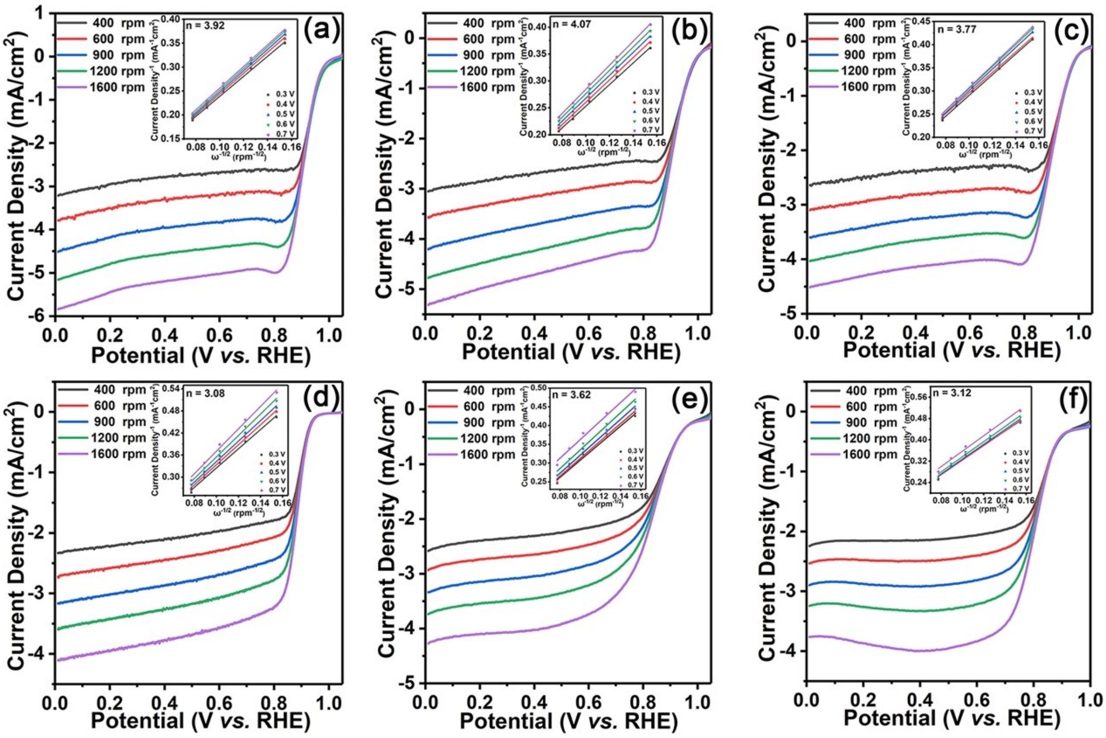

Figure S12 The ORR polarization curves at different rotating rates of (a) Fe-Co_2P@NPDC, (b) Fe-Co_2P@NPDC-2, (c) Fe-Co_2P@NPDC-1, (d) Co_2P@NPDC, (e) NPDC, and (f) NDC.

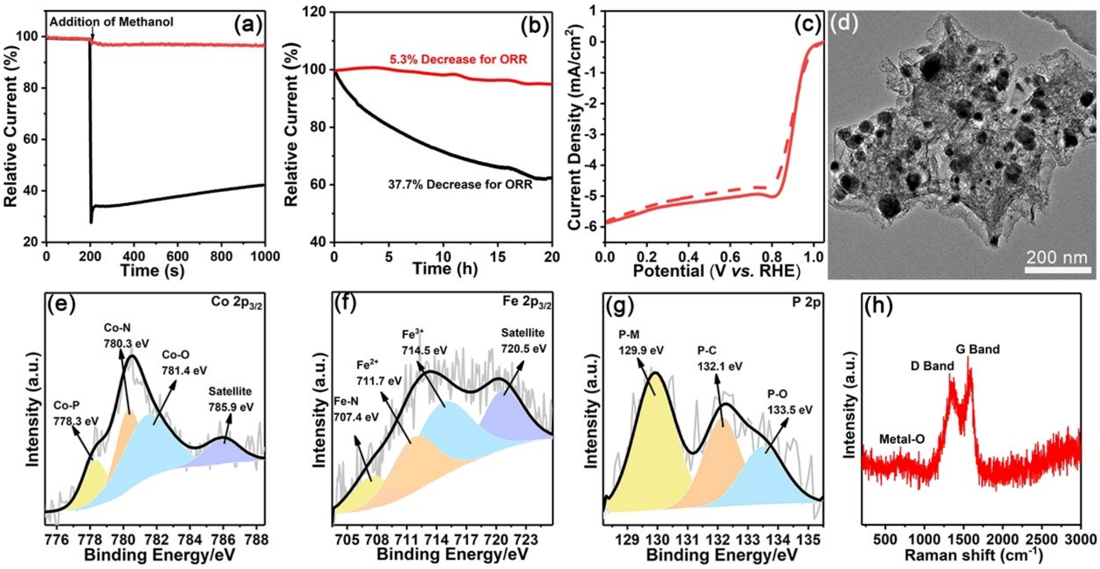

Figure S13 (a) Methanol crossover tolerance for ORR and (b) durability evaluation on *i-t* chronoamperometric responses using different catalysts (0.89 V). Notes: (red) Fe-Co_2P@NPDC, and (black) Pt/C. (c) LSV curves of Fe-Co_2P@NPDC sample before (solid line) and after (dotted line) 20 h operating. (d) TEM image, (e-g) XPS and Raman spectra (h) of Fe-Co_2P@NPDC as ORR catalyst after stability test.

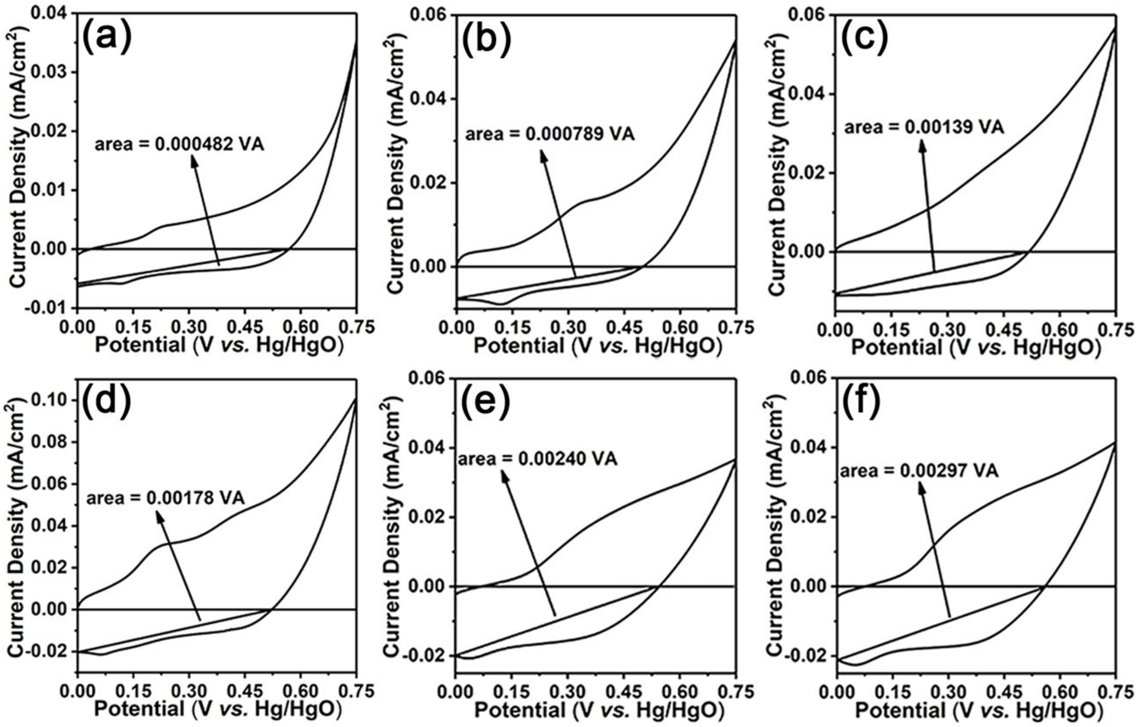

Figure S14 Reduction peaks recorded at 300 mV/s for determination of numbers of surface active sites: (a) Fe-Co_2P@NPDC, (b) Fe-Co_2P@NPDC-2, (c) Fe-Co_2P@NPDC-1, (d) Co_2P@NPDC, (e) NPDC, and (f) NDC.

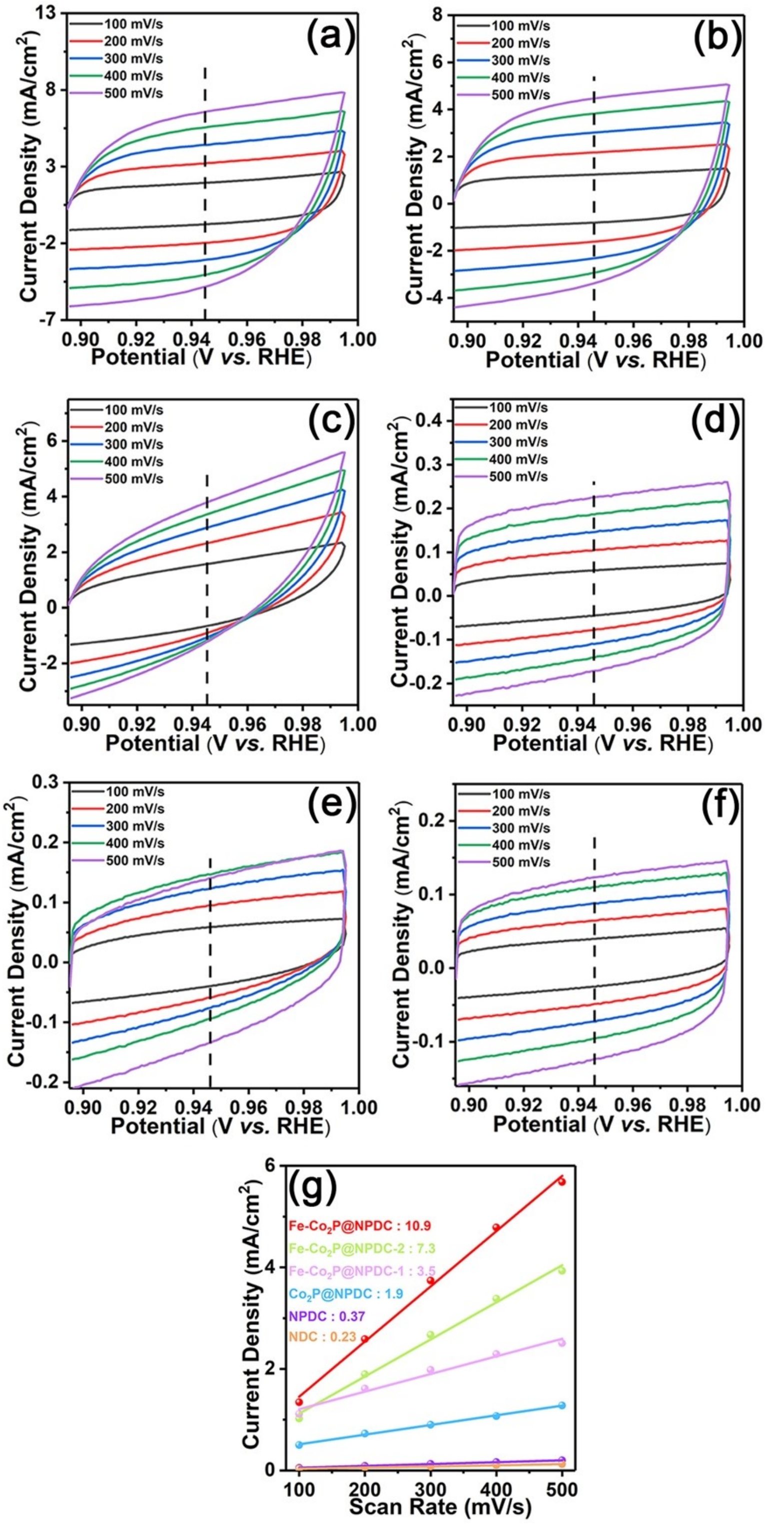

Figure S15 Cyclic voltammograms recorded at increasing scan rates for OER in 1.0 M KOH: (a) Fe-Co_2P@NPDC, (b) Fe-Co_2P@NPDC-2, (c) Fe-Co_2P@NPDC-1, (d) Co_2P@NPDC, (e) NPDC, and (f) NDC; (g) linear fitting of current density difference (recorded at 0.945 V *vs*. RHE) *vs.* scan rate in 1.0 KOH to determine C_{dl}.

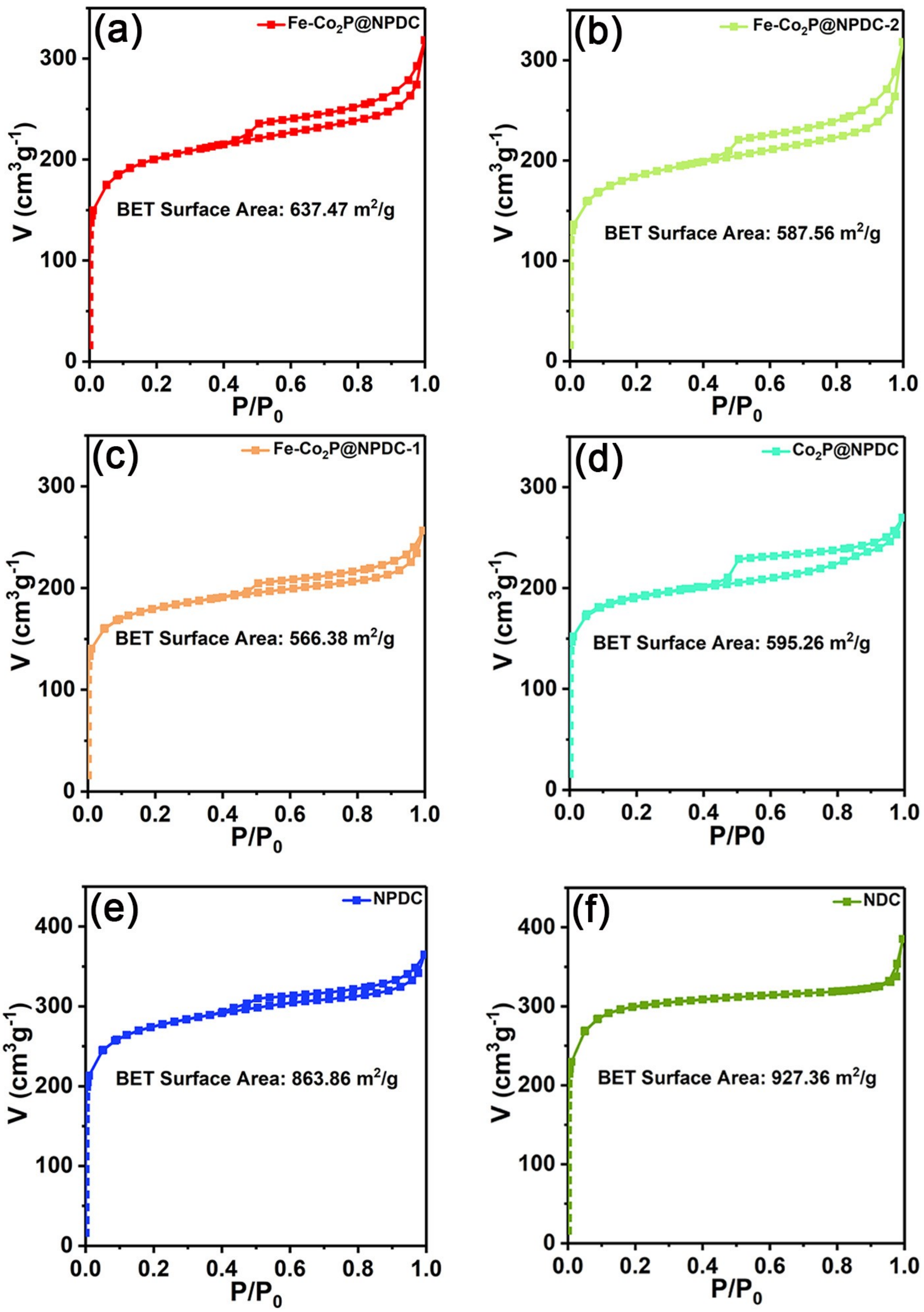

Figure S16 Nitrogen adsorption/desorption isotherms of different catalysts: (a) Fe-Co_2P@NPDC, (b) Fe-Co_2P@NPDC-2, (c) Fe-Co_2P@NPDC-1, (d) Co_2P@NPDC, (e) NPDC, and (f) NDC.

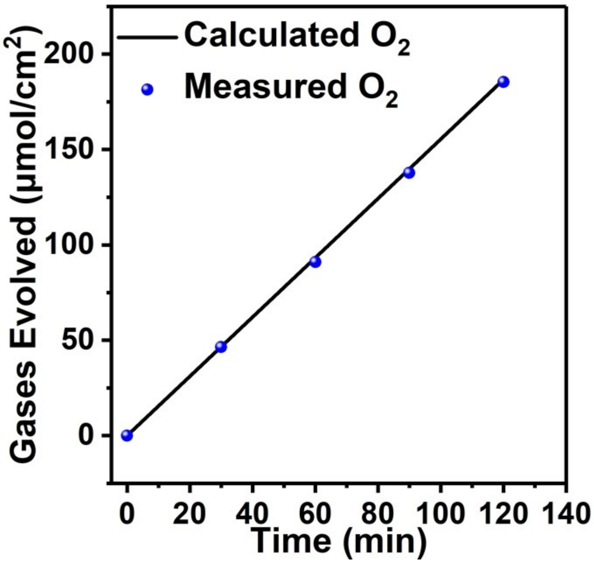

Figure S17 Amounts of O_2 experimentally measured and theoretically calculated *versus* time at a current density of 10 mA/cm^2 with Fe-Co_2P@NPDC as catalyst.

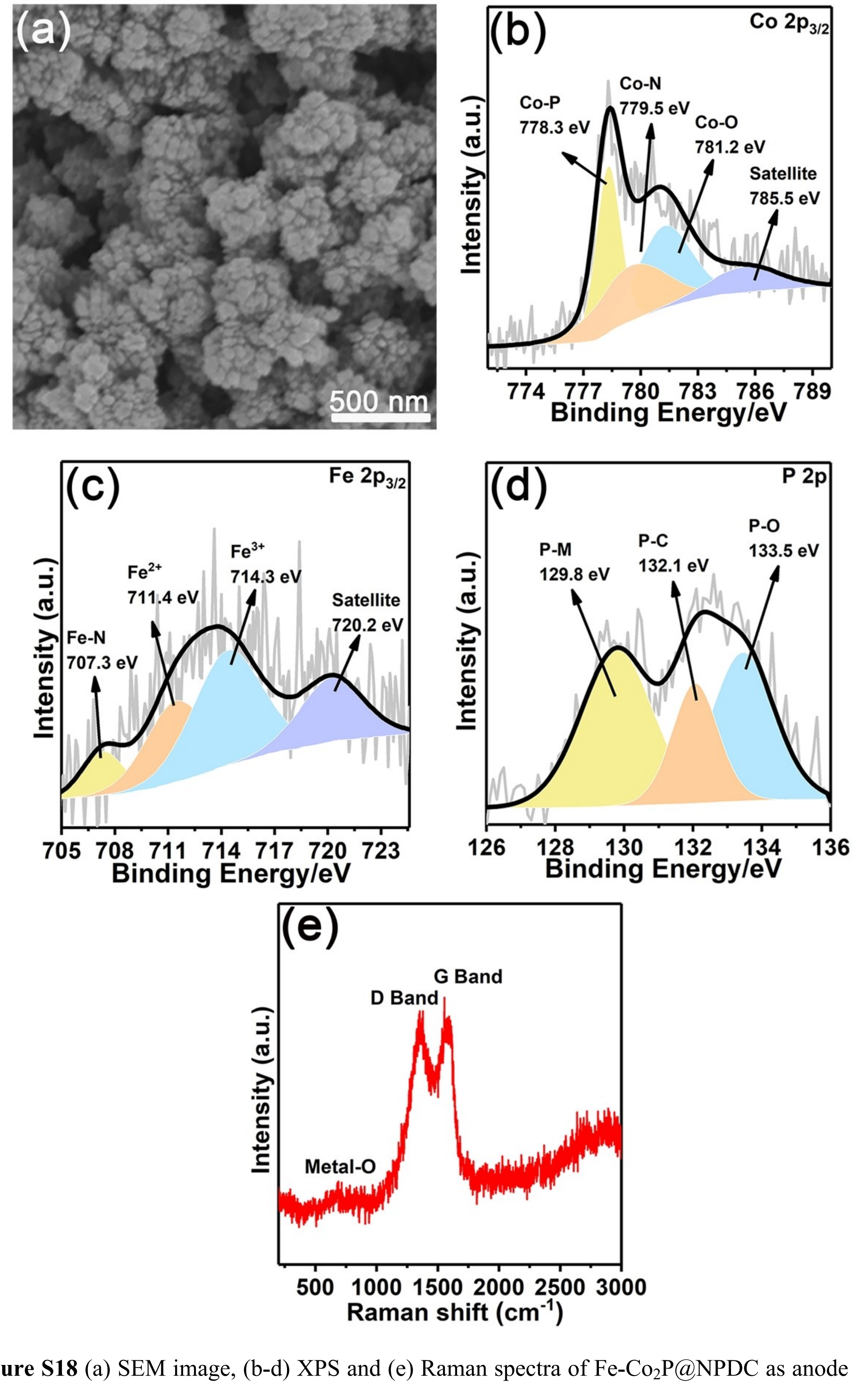

Figure S18 (a) SEM image, (b-d) XPS and (e) Raman spectra of Fe-Co_2P@NPDC as anode OER catalyst after stability test.

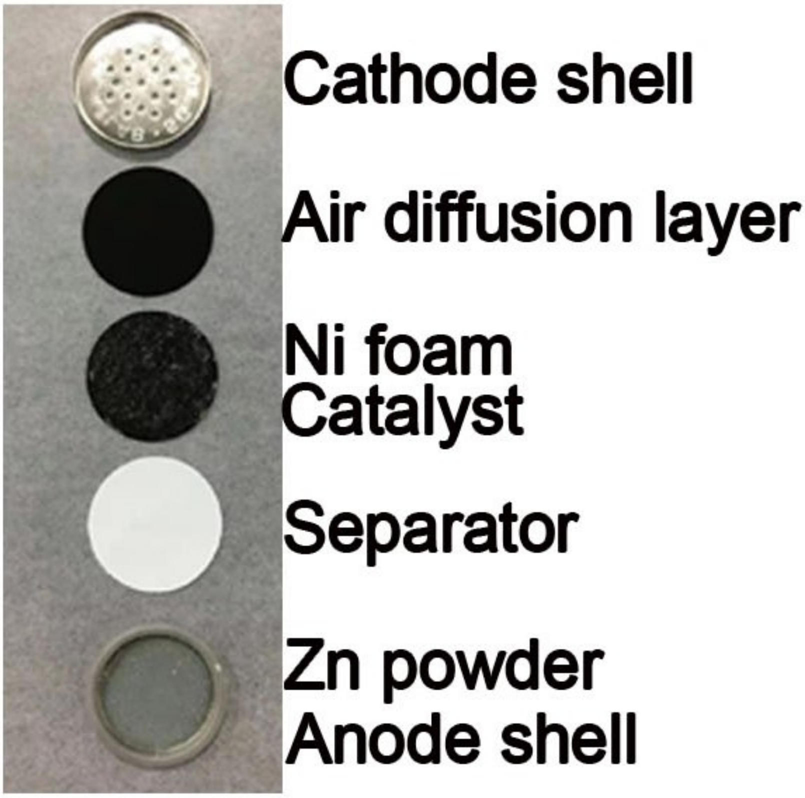

Figure S19 Digital image of the primary button cell Zinc-air battery.

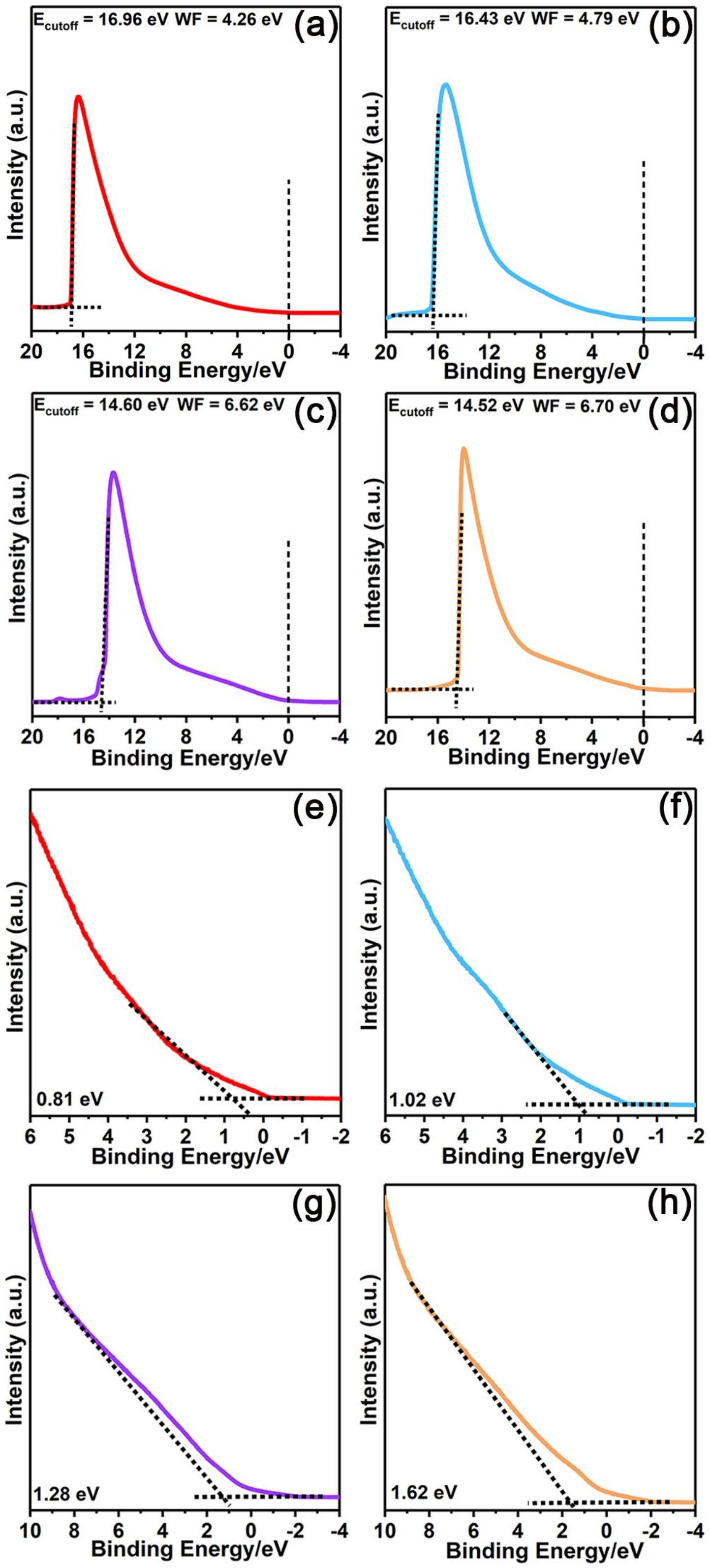

Figure S20 (a-d) working functions and (e-h) valence band maximum values of the as-prepared catalysts. Notes: (red) Fe-Co_2P@NPDC, (shy blue) Co_2P@NDC, (dark purple) NPDC, and (orange) NDC.

Table S1 Comparison of ORR in 0.1 M KOH and OER performances in 1.0 M KOH: present work *vs*. literature.

Catalysts	$E_{1/2}$ **(V) for ORR**	η_{10} **(mV) for OER**	**ΔE (V)**	**References**
Fe-Co_2P@NPDC	**0.895**	**320**	**0.655**	***This work***
FeCo-N-C-700	0.896	370	0.710	S1
Co/N CCPC-3	0.827	401	0.799	S2
(Fe,Co)-SA/CS	0.860	360	0.730	S3
Co_9S_8-NSHPCNF	0.820	350	0.760	S4
Fe/Ni(1:3)-NG	0.840	480	0.868	S5
FeCo/FeN_2/NHOPC	0.860	340	0.710	S6
Fe/Ni-N-C	0.861	322	0.691	S7
FeCo@NC-g	0.890	347	0.690	S8
Mo-N/C@MoS_2	0.810	390	0.810	S9

Table S2 Percentage of different N species in the catalysts.

Catalysts	Pyridinic-N (%)	M-N (%)	Pyrrolic-N (%)	Graphitic-N (%)	Oxidized-N (%)
Fe-Co_2P@NPDC	34.65	20.13	23.40	11.84	9.98
Fe-Co_2P@NPDC-2	37.32	17.60	19.63	18.85	6.60
Fe-Co_2P@NPDC-1	31.57	16.42	19.11	14.17	18.73
Co_2P@NPDC	28.03	15.61	31.60	12.76	12.00

Table S3 Comparison of the peak power density and capacity: present work *vs*. literature.

Catalysts	**Current density (mA/cm^2)**	**Peak power density (mW/cm^2)**	**Capacity (mAh/g at 10 mA/cm^2)**	**References**
Fe-Co_2P@NPDC	**390**	**340**	**762**	***This work***
Co/N CCPC-3	120	87	707	S2
Co_3O_4/MnO_2-CNTs350	273	534	770	S10
Co/Co_2P@NPCNTs	318	190	N/A	S11
Co-NC@Al_2O_3	90	72	530	S12
Co-*N*-PHCNTS	130	125	N/A	S13
Co@Co_3O_4@NC-900	60	64	650	S14
Ni-Fe-MoN NTs	315	118	753	S15
CoS_x@Cu_2MoS_4-MoS_2/NSG	58	40	491	S16

Table S4 Comparison of the rechargeable Zn-air battery performances: present work *vs*. literature.

Catalysts	**Current density (mA/cm^2)**	**Time (h)**	**Voltage gap (V)**	**References**
Fe-Co_2P@NPDC	**1**	**85**	**0.41**	***This work***
FeCo-N-C-700	1	62	0.52	S1
Mo-N/C@MoS_2	1	50	0.98	S9
Co@IC/MoC@PC	1	100	0.41	S17
$Co_{5.47}N$@N-rGO-750	1	40	0.90	S18

Table S5 Percentage of different P species in the catalysts.

Catalysts	P-M (%)	P-C (%)	P-O (%)
Fe-Co_2P@NPDC	16.87	58.90	24.23
Fe-Co_2P@NPDC-2	29.50	38.92	31.58
Fe-Co_2P@NPDC-1	18.87	34.63	46.50
Co_2P@NPDC	49.51	21.83	28.66
NPDC	N/A	26.74	73.26

References

S1 X. D. Duan, S. S. Ren, N. Pan, M. D. Zhang and H. G. Zheng, *J. Mater. Chem. A*, 2020, **8**, 9355-9363.

S2 T. Wang, Y. He, Y. J. Liu, F. J. Guo, X. F. Li, H. B. Chen, H. M. Li and Z. Q. Lin, *Nano Energy*, 2021, **79**, 105487.

S3 V. Jose, H. Hu, E. Edison, W. Manalastas, Jr. H. Ren, P. Kidkhunthod, S. Sreejith, A. Jayakumar, J. M. V. Nsanzimana, M. Srinivasan, J. Choi and J. M. Lee, *Small Methods*, 2021, **5**, 2000751.

S4 W. Peng, Y. Wang, X. X. Yang, L. C. Mao, J. H. Jin, S. L. Yang, K. Fu and G. Li, *Appl. Catal., B*, 2020, **268**, 118437.

S5 Y. Ma, H. Y. Fan, C. Wu, M. D. Zhang, J. H. Yu, L. Song, K. R. Li and J. P. He, *Carbon*, 2021, **185**, 526-535.

S6 Y. Wang, M. F. Qiao and X. Mamat, *Chem. Eng. J.*, 2020, **402**, 126214.

S7 H. G. Li, J. Wang, R. J. Qi, Y. F. Hu, J. Zhang, H. B. Zhao, J. J. Zhang and Y. F. Zhao, *Appl. Catal., B*, 2021, **285**, 119778.

S8 L. B. Huang, L. Zhao, Y. Zhang, H. Luo, X. Zhang, J. A. Zhang, H. Pan and J. S. Hu, *Chem. Eng. J.*, 2021, **418**, 129409.

S9 I. S. Amiinu, Z. Pu, X. Liu, K. A. Owusu, H. G. R. Monestel, F. O. Boakye, H. Zhang and S.

Mu, *Adv. Funct. Mater.*, 2017, **27**, 1702300.

S10 N. N. Xu, Y. X. Zhang, M. Wang, X. J. Fan, T. Zhang, L.W. Peng, X. D. Zhou and J. L. Qiao, *Nano Energy*, 2019, **65**, 104021.

S11 H. Q. Yang, B. D. Wang, S. Q. Kou, G. L. Lu and Z. N. Liu, *Chem. Eng. J.*, 2021, **425**, 131589.

S12 L. Zhu, D. Z. Zheng, Z. F. Wang, X. S. Zheng, P. P. Fang, J. F. Zhu, M. H. Yu, Y. X. Tong and X. L. Lu, *Adv. Mater.*, 2018, **30**, 1805268.

S13 Y. Guan, Y. L. Li, S. Luo, X. Z. Ren, L. B. Deng, L. N. Sun, H. W. Mi, P. X. Zhang and J. H. Liu, *Appl. Catal., B*, 2019, **256**, 117871.

S14 Z. Y. Guo, F. M. Wang, Y. Xia, J. L. Li, A. G. Tamirat, Y. R. Liu, L. Wang, Y. G. Wang and Y. Y. Xia, *J. Mater. Chem. A*, 2018, **8**, 1443-1452.

S15 C. L. Zhu, Z. X. Yin, W. H. Lai, Y. Sun, L. N. Liu, X. T. Zhang, Y. J. Chen and S. L. Chou, *Adv. Energy Mater.*, 2018, **8**, 1802327.

S16 D. C. Nguyen, D. T. Tran, T. L. L. Doan, D. H. Kim, N. H. Kim and J. H. Lee, *Adv. Energy Mater.*, 2020, **10**, 1903289.

S17 L. Zhang, Y. X. Zhu, Z. C. Nie, Z. Y. Li, Y. Ye, L. H. Li, J. Hong, Z. H. Bi, Y. T. Zhou and G. Z. Hu, *ACS Nano*, 2021, **15**, 13399-13414.

S18 X. X. Shu, S. Chen, S. Chen, W. Pan and J. T. Zhang, *Carbon*, 2020, **157**, 234-243.